High Power Laser Science and Engineering, (2024), Vol. 12, e7, 14 pages.
doi:10.1017/hpl.2023.86

HIGH POWER LASER SCIENCE AND ENGINEERING

RESEARCH ARTICLE

Energy enhancement of laser-driven ions by radiation reaction and Breit–Wheeler pair production in the ultra-relativistic transparency regime

Shikha Bhadoria[1,2], Mattias Marklund[2], and Christoph H. Keitel[1]

[1] *Max-Planck-Institut für Kernphysik, Heidelberg, Germany*

[2] *Department of Physics, University of Gothenburg, Göteborg, Sweden*

(Received 11 August 2023; revised 7 October 2023; accepted 9 November 2023)

Abstract

The impact of radiation reaction and Breit–Wheeler pair production on the acceleration of fully ionized carbon ions driven by an intense linearly polarized laser pulse has been investigated in the ultra-relativistic transparency regime. Against initial expectations, the radiation reaction and pair production at ultra-high laser intensities are found to enhance the energy gained by the ions. The electrons lose most of their transverse momentum, and the additionally produced pair plasma of Breit–Wheeler electrons and positrons co-streams in the forward direction as opposed to the existing electrons streaming at an angle above zero degree. We discuss how these observations could be explained by the changes in the phase velocity of the Buneman instability, which is known to aid ion acceleration in the breakout afterburner regime, by tapping the free energy in the relative electron and ion streams. We present evidence that these non-classical effects can further improve the highest carbon ion energies in this transparency regime.

Keywords: ion acceleration; quantum electrodynamic effects

1. Introduction

Accelerated ion beams have a multitude of applications ranging from nuclear reactions induced by energetic heavy ions[1] to fast ignition fusion[2,3], aiding neutron production[4] and also hadrontherapy for cancer treatment[5–7]. Laser-driven ion acceleration has received much attention in recent decades, as it offers the possibility of having alternate accelerators that are smaller and more affordable as opposed to the conventional linacs, cyclotrons and synchrotron[8,9]. Experimental demonstration of ion beams by several mechanisms exhibiting different performances, such as target normal sheath acceleration (TNSA)[10], radiation-pressure acceleration (RPA)[11–13], collisionless shock acceleration (CSA)[14,15], the breakout afterburner (BOA)[16–19], etc., has already been achieved[20]. Significant efforts of innovative laser/target configurations have also been made to push the number of ion beam characteristics (energies and flux)[21], yet the highest gained energy is still less than 100 MeV/u[20,22,23]. Nevertheless, the prospects of achieving even higher ion energies with the next generation of laser sources are promising[24].

Correspondence to: Shikha Bhadoria, Department of Physics, University of Gothenburg, 40530 Göteborg, Sweden. Email: shikha.bhadoria@physics.gu.se

The BOA is one of the high-performance laser-driven ion-acceleration mechanisms capable of accelerating ions to relatively higher values even with state-of-the-art lasers. In this, an initially opaque, ultra-thin target (width around laser skin depth) turns transparent to the incoming laser pulse, due to lowering of the density by the expanding plasma and increase in critical density by the electron's relativistic motion (relativistically induced transparency, RIT)[16,25]. This leads to a phase of extreme ion acceleration (BOA phase), which continues to exist until the electron density of the expanding target becomes classically underdense[26]. Buneman instability (in single ion-species targets) and ion–ion acoustic instability (in the case of multispecies targets[27]) result in an electrostatic mode structure, which is found to be instrumental in transferring the laser energy to ions via laser-induced electronic drifts[17,28]. The efficiency of this mechanism is maximized when the peak of the laser pulse arrives precisely at the onset of relativistic transparency[18,29], as opposed to the RPA-light-sail mechanism, which requires opacity in ultra-thin targets.

Experimental demonstration of fully ionized carbon ion acceleration via the BOA mechanism up to 40–50 MeV/u has been achieved using approximately 50–250 nm thick targets with the TRIDENT laser and the Texas Petawatt laser facility[18]. Also, simultaneously existing TNSA and BOA

signatures in proton spectra (energy ~ 61 MeV) have been identified at the PHELIX laser facility at GSI with 200–1200 nm targets with a 4×10^{22}–8×10^{22} W/cm^2 laser[30]. Recently measured 30 MeV carbon ions in the transparency regime were shown to be accelerated by extremely localized axial fields at the J-KAREN-P facility (also complemented by experiments at DRACO-PW)[31]. Much more intense and powerful lasers, such as ELI and APOLLON, are soon to surface[32–34] (as expected in the laser-power timeline and also with the recent prototype design using wide-angle non-collinear optical parametric chirped pulse amplification (WNOPCPA) allowing a 0.5 EW system[35]) and can further improve these numbers, as they will allow a larger laser energy transfer to the ions.

However, in the ultra-relativistic regime other quantum electrodynamic dynamic (QED) effects become non-negligible when the electric field of the laser in the electron's rest frame gets closer to the critical Schwinger field ($E_s = 1.3826\times10^{18}$ V m^{-1}[36]). The most important effects are high-frequency radiation emission by electrons pushed in the laser-field (with a consequent back reaction on individual electrons, the radiation reaction (RR)) and the multi-photon Breit–Wheeler (BW) process leading to the generation of electron–positron pairs[37]. These QED effects, usually expected to deplete energy from a physical system[38–42], may though significantly modify the collective plasma dynamics[43] with yet unexplored indirect effects on the ion energy.

In this paper, the impact of both RR and non-linear BW pair production (PP, $\gamma + n\gamma \rightarrow e^-e^+$) on the acceleration of ions in the transparency regime has been investigated using particle-in-cell (PIC) simulations. An increase in ion energies by RR alone in the transparency regime has already been reported[39,40,44–47], although these neglect the stochastic nature of high-energy photon emission. Here, we show evidence that in this regime, both RR and PP together can lead to a notable improvement of up to 30% in the ion energy beyond previous results. This is attributed to more collimation of the plasma stream due to QED effects. Although the co-existence of a less-efficient RPA cannot be ruled out[48], we present a discussion on how the observed spectra could also be explained via the BOA mechanism by identifying low-frequency electrostatic modes in the spectral analysis of the system. Then the improvement in ion energies is explained by an enhancement of the phase velocity of the relativistic Buneman instability (RBI), which is responsible for accelerating ions via Landau damping[49]. This allows for an efficient energy transfer from the laser to the ions facilitated by electron flow during the onset of RIT.

2. Simulations

We performed 2D PIC simulations using both the open-source codes EPOCH (in Sections 3 and 4) and SMILEI (in Section 3.1 and Appendix B), which include quantum RR and PP by the probabilistic Monte Carlo method[50,51]. We employ a linearly s-polarized laser pulse, impinging on the left-hand boundary with a finite spatio-temporal profile $I(t,y) = I_0 \exp(-\left((y-y')/r_0\right)^2)\exp(-\left((t-t')/\tau_0\right)^2)$, with $r_0 = 3\,\mu$m, $y' = 4\,\mu$m, $\tau_0 = 40$ fs, $t' = 30$ fs. The laser peak intensity of $I_0 = 4.95\times10^{23}$ W/cm^2 might soon be realizable[52], giving $a_0 = eE/m_e\omega c = 600$, where e is the electronic mass, ω is the laser frequency and c is the velocity of light in a vacuum. The polarization of the laser is chosen to be s-polarized as here our 2D simulations are then closer to 3D scenarios, as opposed to p-polarized laser light, which can artificially heat electrons and can exaggerate the effectiveness of ion acceleration in such a scenario[39,40,44,53]. It interacts with a pre-formed fully ionized carbon plasma (C^{6+}[18,25]) with a temperature $T_{e^-} = T_{C^+} = 1200$ eV and density $n_{e^-} = 200n_c$, where $n_c = m_e\omega^2/4\pi e^2$ is the classical critical density of a plasma for 1 μm laser wavelength. The target has a thickness of 0.6 μm and is located at 12 μm from the left-hand boundary of the simulation box. We employ transmitting and periodic boundary conditions in the x and y directions, respectively. The simulation box has dimensions of $L_x \times L_y = 50\,\mu\text{m}\times 8\,\mu\text{m}$, with the cell size of $\Delta_x \times \Delta_y = 10\text{ nm}\times 10\text{ nm}$ using 85 particles per cell.

Laser–solid pair creation by QED processes mediated in coulombic fields, such as Bethe–Heitler (BH)[54] and trident (tri) processes[55,56] is not considered in these simulations. This should be reasonable as the ratio of the electric field strength of the laser to that of the atomic nucleus at ionic Debye length is 10^3 (using average fields at a Bohr radius for $Z = 6$ being $\langle E\rangle \sim 4\times10^{14}$ V/m[57]), favouring pair creation by photon–laser interaction over photon–nuclear interaction. Also with the sub-micrometre target of ion density of $(200/Z)n_c$, the pair creation probability due to the ionic nuclear field should be lower, as also shown in Ref. [58]. In this scenario, $n_{BW}/n_{tri} \sim 210$ while $n_{BW}/n_{BH} \sim 53$ (see Appendix B). In this paper, we study PP only by the BW process. We also performed parameter scans with the same laser but different target densities $[60, 100]n_c$ and observed a similar improvement by QED effects only for $100n_c$. In a near-critical thin target 0.6 μm, $a_0 = 540$, $n_e = 500n_c$, the QED effects were observed to reduce ion energies (as in Ref. [38]). Determining an optimum density range for a high laser parameter a_0 where QED effects enhance the ion energies would call for a deliberate large-scale parameter scan (as in Ref. [59]).

3. Dynamics

The laser-field pushes hot electrons inside the target forward that quickly reach the non-irradiated side (rear) of the target faster than the ions. This sets up a very brief TNSA field there that kickstarts the ion acceleration from the TNSA

https://doi.org/10.1017/hpl.2023.86 Published online by Cambridge University Press

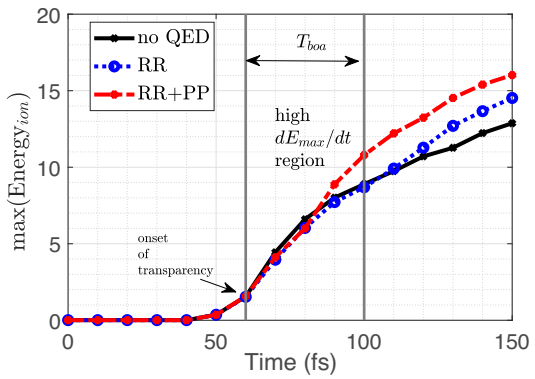

Figure 1. The 1D plot shows the maximum energy gained by ions $E_{\max}$ (in GeV) with time t in all three cases labelled. Here, a region in time is identified as T_{boa}, which starts at the onset of transparency and extends until the enhanced ion acceleration slows down (after which the slope of maximum ion energy begins to change to a smaller value).

mechanism at around 50 fs. The electrons oscillate with relativistic velocity and, thus, the effective critical density is reduced.

Moreover, as the recirculating hot electrons heat the target up, it begins to expand and the density lowers further. The target then begins to become relativistically transparent and the laser is able to penetrate through it. This marks the onset of transparency (at $\sim$ 60 fs) where the streams of electrons and ions co-move with the penetrating laser and are susceptible to the occurrence of the BOA. In a realistic scenario of a laser interacting with a thin foil, there can be multiple co-existing accelerating fields/mechanisms that can be broadly disentangled in time.

In Figure 1, we plot the maximum energy gained by ions ($E_{\max}$ in GeV) as a function of time (t) in all three cases, which are labelled (when QED effects are artificially turned off, when only RR is included and when PP is also included, RR+PP). The angular distribution of ions is not contained in this figure and one cannot distinguish the on-axis and off-axis ions here. Yet, we broadly identify three stages of ion acceleration.

Stage 1 is pre-transparency time (up to 60 fs) when the target is still intact and ion acceleration occurs with the combination of TNSA and RPA very briefly. This is determined from simulations when at least some focal part of the target becomes completely transparent to the laser and it passes through.

After around 60 fs, ion acceleration enters Stage 2, which we refer to as the BOA phase (marked as T_{boa}). Here electrons and ions co-stream with the laser and the system could be susceptible to RBI. This can also be seen in Figure 2, where the 2D spatial distribution of electrons ($n_{\text{e}}\,(x,y)$ on the top row, panels a(i)–d(i)) and ions ($n_{\text{i}}\,(x,y)$ on the bottom row, panels a(ii)–d(ii)) in the T_{boa} region is presented. Here we only present the time evolution of electrons and ions in x-y space for the no-QED case to describe the timing of the dynamics. The QED effects were not very well distinguishable in this space. As will be seen in later sections the QED cases are clearly distinguishable from the no-QED case when visualized in angular-energy space. It is clear from these subplots in Figure 2 that the electrons and ions are in close spatial proximity in Stage 2. The relative velocity between electron and ion flows acts as a source of free-energy for low-frequency electrostatic modes such as RBI to develop. In Stage 2, ions could be accelerated by this growing mode. Due to the Gaussian spatial profile of the laser, the electrons and ions stream at an angle as they move slightly away from the focal spot region. The approximate times of Stage 2 are defined as follows: Stage 2 is characterized by a high rate of change in maximum ion energies and extends until the enhanced-ion acceleration slows down (after around 100 fs the slope of maximum ion energy begins to clearly change to a smaller value). So, Stage 2 is from the onset of transparency to saturation in the rate of energy gain in the ions. Stage 1 witnesses the large

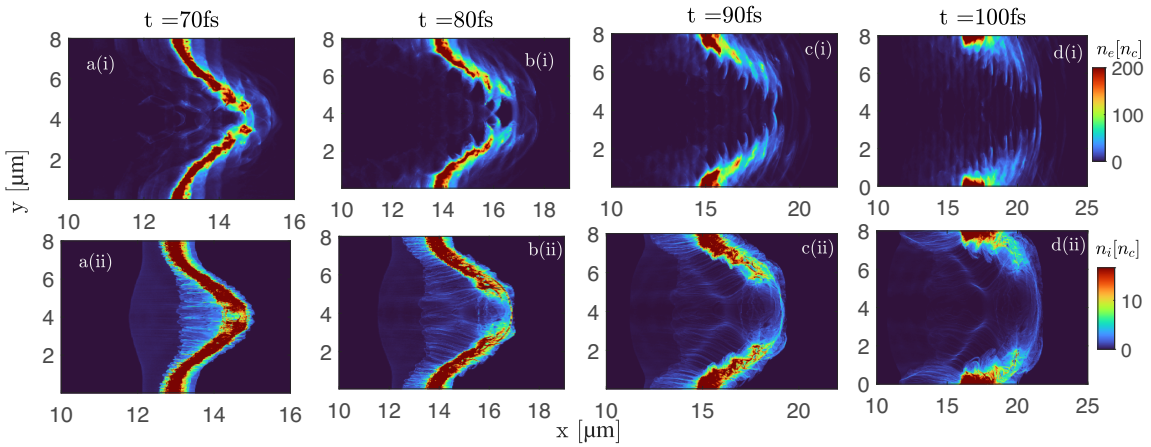

Figure 2. These subplots show 2D spatial distributions of electrons (top row, a(i)–d(i)) and ions (bottom row, a(ii)–d(ii)) in the T_{boa} region (only no-QED case shown).

https://doi.org/10.1017/hpl.2023.86 Published online by Cambridge University Press

production of high-energy photons and pairs that saturate in Stage 2 (also see Appendix A, Figure 9).

Afterwards, ion acceleration enters into Stage 3, where electrons are significantly expelled and acceleration occurs due to Coulomb explosion, as also seen in Ref. [60]. In this paper, we focus on Stage 2 of ion acceleration as this is not only the stage of rapid energy gain dominating the overall accelerating mechanisms, but also the stage where QED effects reverse their energy-reduction trend from its preceding stage.

4. Early stage dynamics

4.1. Electrons

Figure 3 shows the electron's energy-angle distribution at 80 fs (BOA phase) where the laser pulse has already penetrated the target (injecting electrons into vacuum laser acceleration by relativistic transparency[61]). Figure 3(a) shows the case where the QED effects are artificially turned off, Figure 3(b) shows the case when RR is included in the plasma dynamics and Figure 3(c) shows the case when both RR and PP are included. One can clearly see in Figure 3(a) that electrons stream diffusely at an angle and gain energy. The majority of the electrons stream in the forward direction (laser-propagation direction) and a small percentage of electrons also gain energy at the back (∼180°). In Figure 3(b), when RR is also included, the electrons become more forward-directed and the backward acceleration is suppressed. The latter observation is expected, that is, the electrons that counter-propagate the incoming laser experience Doppler-upshifted fields leading to a substantial suppression of the backward acceleration (also observed in Refs. [38–40, 45]). As the laser-accelerated electrons lose part of their energies in high-energy-photon emission, the overall divergence of the electron's angular distribution reduces as they get pushed forward with the laser. A similar reduction in the electron's transverse momentum and electron cooling due to the RR is also seen in Refs. [39, 40, 46, 62]. Although laser collision with an electron-beam with a quantum RR is shown to increase the electron energy distribution[63], here the overall impact is not dominated by stochasticity (see the next section).

4.2. Stochasticity in the RR case

In order to isolate the stochastic aspect of the RR from only the continuous frictional drag on particles, we carried out one simulation that models the RR with a corrected Landau–Lifschitz model that excludes the stochastic nature of photon emission (using SMILEI code). Figure 4 shows the electron's momentum phase-space distribution in the no-QED case (Figure 4(a)), with the RR modelled by the corrected Landau–Lifschitz method (Figure 4(b)) and the RR modelled by the Monte Carlo method (Figure 4(c)).

Comparing Figures 4(b) and 4(c), we see that a significant reduction in the electron's transverse momentum with the RR is common in both. Figure 4(c), which also captures stochastic effects of the RR, seems to extend the electron's momentum in both the longitudinal and transverse directions. This is actually consistent with Ref. [63], which shows that stochasticity leads to a greater spread of the electron energy distribution. Clearly in this scenario, the collimation of electrons due to the leading term of the Landau–Lifschitz RR force ('drift term') dominates over the spreading out of electrons due to the stochastic ('diffusion term') effects, such that, compared to the no-QED case, there is an overall collimation of the beam. The subsequent ion energies due to stochastic effects are discussed in Appendix D.

4.3. Additional pair plasma

In Figure 3(c), when the RR+PP both are included, apart from a more collimated stream of electron fluid, here one can also see a higher density of electrons that also gain larger

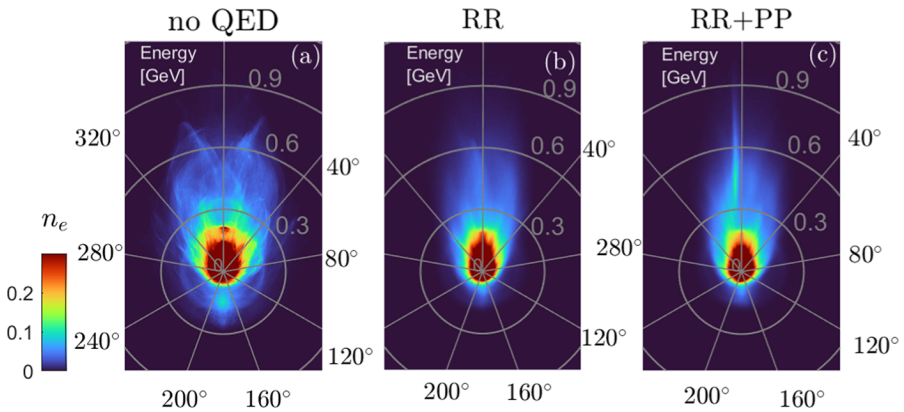

Figure 3. Energy-angular distribution of electrons (in a.u.) in the BOA phase without radiation reaction (a), with radiation reaction (b) and with pair production as well (c) (excluding the produced Breit–Wheeler electron density) at 80 fs.

https://doi.org/10.1017/hpl.2023.86 Published online by Cambridge University Press

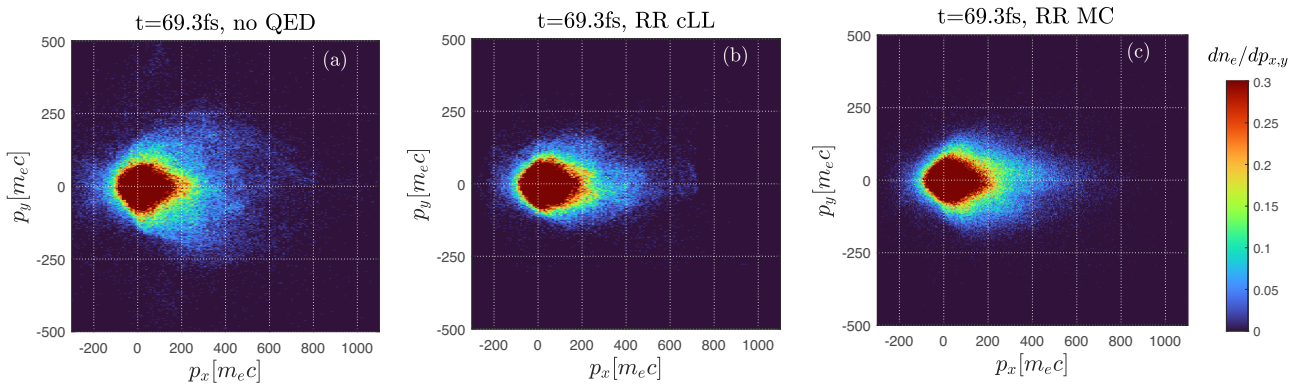

Figure 4. The electron phase space in the no-QED case (a), the RR modelled by the corrected Landau–Lifschitz (LL) method (b) and the RR modelled by the Monte Carlo method (c) at the onset of the BOA phase.

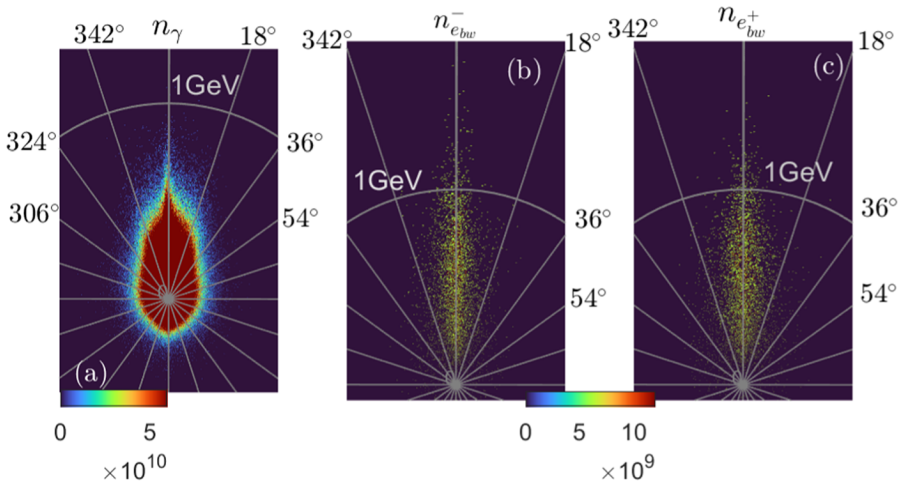

Figure 5. Energy-angle distribution of photons (a), BW electrons (b) and BW positrons (c) at 80 fs.

energy (around 0.6 GeV). This is due to the production of the BW pairs that occurs due to the interaction of laser photons with the emitted gamma-ray photons. One can clearly see that the created pairs have higher maximum energy than the target electrons. The angularly streaming target electrons gain more energy from the newly formed energetic pair plasma at 0° as all species of similar masses exchange energies. This leads to additional collimation of the electron stream with the production of pairs.

Figures 5(a)–5(c) show the energy-angle distribution of photons, BW electrons and BW positrons, respectively, in the RR+PP case at 80 fs. One can clearly see a large number of gamma-ray photons in the laser-propagation direction being produced in Figure 5(a) as the target turns transparent and the laser is allowed to interact with prolific electrons. In Figures 5(b) and 5(c), we see the high-energy and forward-streaming pair plasma that is responsible for the higher energy and density of electrons in Figure 3(c). Since the target is already transparent, these pairs do not accumulate at the target region and are unable to shield the incoming laser as in the cushioning scenario[64]; rather, they stream forward with the laser pulse and the ambient plasma.

4.4. Ions

Figure 6 shows the ion distribution in the same fashion as in Figure 3 and at the same time. In the no-QED case in Figure 6(a), the ions with the highest energy (around 6.5 GeV) are off the axis of laser polarization or propagation, as also seen in Ref. [65]. This occurs at 80 fs when RBI could operate, which is a low-frequency high-amplitude electrostatic mode that feeds on the relative flow velocity between electrons and ions and accelerates ions with a wave-particle resonance mechanism[17,49]. In the same figure, one may also see some ions with approximately 5.7 GeV energy that are on the laser-propagation axis. This is when the off-axis ion streams mutually interact.

In Figure 6(b), the highest gain in energy and the angular divergence of these high-energy ions are reduced at 80 fs when the BOA mechanism could be at play. The on-axis

https://doi.org/10.1017/hpl.2023.86 Published online by Cambridge University Press

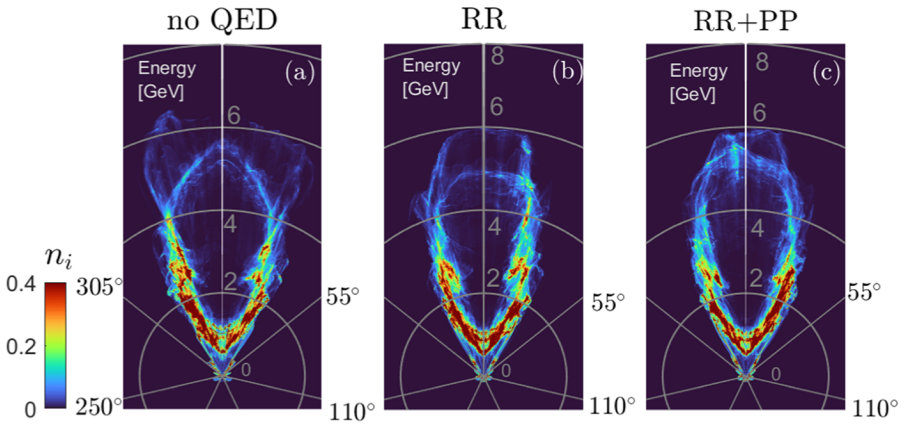

Figure 6. Energy-angle distribution of carbon ions in the BOA phase without the radiation reaction (a), with the radiation reaction (b) and with pair production as well (c) at 80 fs.

and off-axis ions gain nearly the same energies in this case. Further, in Figure 6(c), the angular divergence of the ions is even smaller, and the on-axis ions gain much higher energy (∼5.8 GeV) than the off-axis ones (∼4.6 GeV). The high-energy, on-axis ion bunch is accelerated due to a similar electron bunch in Figure 3(c) on account of the pair plasma (Figure 5(c)). The role of the RBI in these bunches of high-energy ions seems relevant in the higher acceleration of ions. Further, in this paper, we shall present hints as to how certain ions gain higher velocities because they are resonant with the phase velocity of this plasma instability (RBI). The expanding TNSA ions, target electrons and the BW pairs stream forward with the laser and the free energy in the particle streams gives rise to the electrostatic mode, the RBI, that resonates with the ions, allowing them to be rapidly accelerated. The energy loss by electrons is constantly filled up by the long-pulse laser. This beam-like expanding plasma is susceptible to the growth of the RBI, where the phase velocity of the instability is comparable to the highest accelerated velocities of the ions[17].

It should be noted that this scenario could be similar to that of directed coulomb explosion[60] where RPA precedes the later coulomb explosion stage for the acceleration of ions. Although here a higher transparency with higher a_0 with transverse target expansion would reduce the RPA's efficiency[48], there may be a more complex interaction here with a phase of hybrid RPA–BOA accelerating ions from the off-focal opaque part and the focal transparent part of the target, respectively. Confirming an exact composite-accelerating mechanism calls for an investigation of shorter time-scale particle dynamics for the classical case itself, especially with QED effects enhancing ion energies. However, here we limit ourselves only to a discussion on the analysis of the longitudinal electrostatic field structure (similar to Refs. [16, 17, 27]) where we look for the existence of signatures of the RBI.

5. Transparency stage

5.1. *Identifying the RBI from simulation*

The Fourier analysis of the longitudinal electric field from the simulations can shed light on the electrostatic structure of the accelerating fields in the transparency region. This has been performed for all three cases and is shown in Figure 7. Figures 7(a)–7(c) show $|E_x(\omega, k)|^2$ in log scale for the no-QED case, with the RR and with the RR+PP, respectively. The Fourier window has been chosen to be [50, 140] fs and [10, 50] μm to capture the salient features of the instability dynamics in the BOA phase. The BOA time window ($t_{\rm boa} \in$ [60, 100] fs) is identified by the time when we observe rapid ion acceleration ($\sim 2-4$ times in every 10 fs) in our simulations, after which the rate of ion acceleration becomes smaller ($\sim 1-1.1$ times in every 10 fs, as seen in Figure 1).

This BOA window is well within the resolution of the Fourier window shown in Figure 7. In this power spectrum in Figure 7, two distinct low-frequency branches can be clearly identified in all three panels (Figures 7(a)–7(c)). Clearly, one primary branch (labelled *A*) has a higher slope and energy than the other (labelled *B*). The primary branch *A* intersecting the origin is identified as the growing RBI[16]. This branch could also be clearly identified even when we chose smaller windows at earlier times, such as $t \in [50, 80]$ fs or $t \in [50, 100]$ fs (not shown here), with lower phase velocities than the ones shown here. The phase velocity of this branch is seen to increase as we increase the temporal Fourier window within $t_{\rm boa}$, consistent with Ref. [49].

The lower, diffuse and less-powerful branch *B* appears only some time after ($t \in [50, 90]$ fs onwards) the appearance of the primary branch. These two branches merge slightly in Figure 7(a). Looking at Figures 7(b) and 7(c), one can broadly see that the branch *A* is more powerful in both QED cases than in Figure 7(a) (even more in the RR+PP case).

https://doi.org/10.1017/hpl.2023.86 Published online by Cambridge University Press

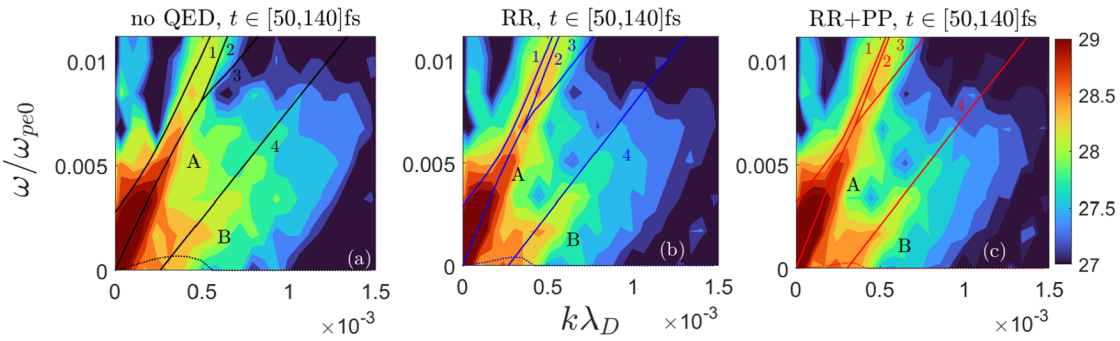

Figure 7. Spectral power as a function of wave number (normalized by Debye's length with initial temperature) and frequency (normalized by plasma frequency), $|E_x(\omega,k)|^2$, in log scale for $t \in [50, 140]$ fs and $x \in [10, 50]$ μm for all three cases (no-QED (a), RR (b) and RR+PP (c)) obtained from the simulations. The real and imaginary roots of Equation (1) (solid and dotted lines, respectively) are over-plotted to facilitate comparison.

Moreover, branch *B* becomes notably more distinct in Figure 7(b) and marginally even more in Figure 7(c). This may be due to the fields generated by the angularly drifting plasma streams that mutually interact, leading to the high-energy on-axis ions seen in the tip of the bubble-like form that the ions make in Figure 6 (potentially a mode harnessing the free energy in off-axis high-energy ion streams). As the radiatively cooled electrons become more forward-directed in QED cases (Figures 3(b) and 3(c)), the angular separation between the streaming plasma ions also lowers. This allows more interaction between the streams and thus branch *B* becomes more distinct. An additional lowering of this angle due to pairs produced at 0° makes this branch *B* stronger in Figure 7(c).

5.2. *RBI from linear theory*

The dispersion relation of the RBI[17] from the linear kinetic theory assuming relativistic cold angularly streaming plasma for the instability is given as follows:

$$\sum_{s=\mathrm{e,i}} \frac{\omega_{\mathrm{p},s}^2\left[1+(p_s\sin\theta_s/m_sc)^2\right]}{k^2\gamma_s^3\left(v_\phi - v_s\cos\theta_s\right)^2} = 1, \qquad (1)$$

where $\omega_{\mathrm{p},s}$ is the plasma frequency, v_s/p_s are the stream velocity/momentum,v_ϕ is the phase velocity (ω/k), γ_s is the respective Lorentz factor and θ_s is the angle of drift, with $s = \mathrm{e,i}$ denoting the electronic and ionic streams, respectively. Although one cannot deny that the perturbative approach might not be the most sophisticated approach to study this, it is the best non-simulation approach available that can facilitate a deeper understanding of such a complex interaction. The dispersion relation of this instability in Equation 1 has been solved and the four roots of the quartic equation have been over-plotted in Figure 7. The input plasma parameters (average electron and ion density, angles of streams and energies) have been extracted from the simulations in each case at around 70 fs when the BOA could be active (see Appendix A)[66].

It should be noted that we use the same dispersion relation for QED cases (Figures 7(b) and 7(c)) as well. This simplified treatment is still reasonable because we carefully choose the plasma parameters at the time after the production of photons and pairs has mostly saturated (see also Section 3). The major impact of the RR and PP is still well captured in the form of changes in the plasma distribution function extracted from the simulation that already includes probabilistic photon emission in plasma evolution. There are two real and two complex roots of this equation, including one high-frequency real root (starts with a positive frequency, as also in Refs. [17, 67]) and the other low-frequency real root (the negative frequency at $k = 0$ crosses the $\omega = 0$ axis as the wave number increases). The other two roots are complex conjugates with the same $\Re(\omega)$ until the non-zero imaginary part vanishes, after which the real parts bifurcate. The positive imaginary part (dotted line in Figure 7) is the unstable mode, while the negative (damped mode) is not shown here.

A good match between branch *A* (from simulation) and the real part of the growing complex root from linear kinetic theory (over-plotted solid line) is visible in all three panels. The phase velocity of the primary branch ($v_\mathrm{p} \sim 0.84c$ in Figure 7(a)) is comparable to the ion velocities attained by the off-axis ions ($v_\mathrm{i} = 0.86c$, $\epsilon_\mathrm{i} \sim 11.26$ GeV), hinting at the possibility of the instability playing a role in the ion acceleration. The instability growth rate progressively lowers and the bifurcation of the roots shifts to lower k values, respectively, which is as expected[49,67]. A lower angle and higher energies of the electron stream (see Figure 3) are also shown to enhance the phase velocities of the RBI wave[49]. As we have seen already in Section 3 that the RR and RR+PP lead to a much more collimated plasma stream in Stage 1 of acceleration (Section 3), a higher phase velocity of the RBI with these QED effects is understandable.

Thus, from the spectral plots it is clear that the RR and RR+PP would enhance the RBI on account of a radiatively cooled more forward-directed electron and ion beam. Interestingly, the low-frequency real root of the same

https://doi.org/10.1017/hpl.2023.86 Published online by Cambridge University Press

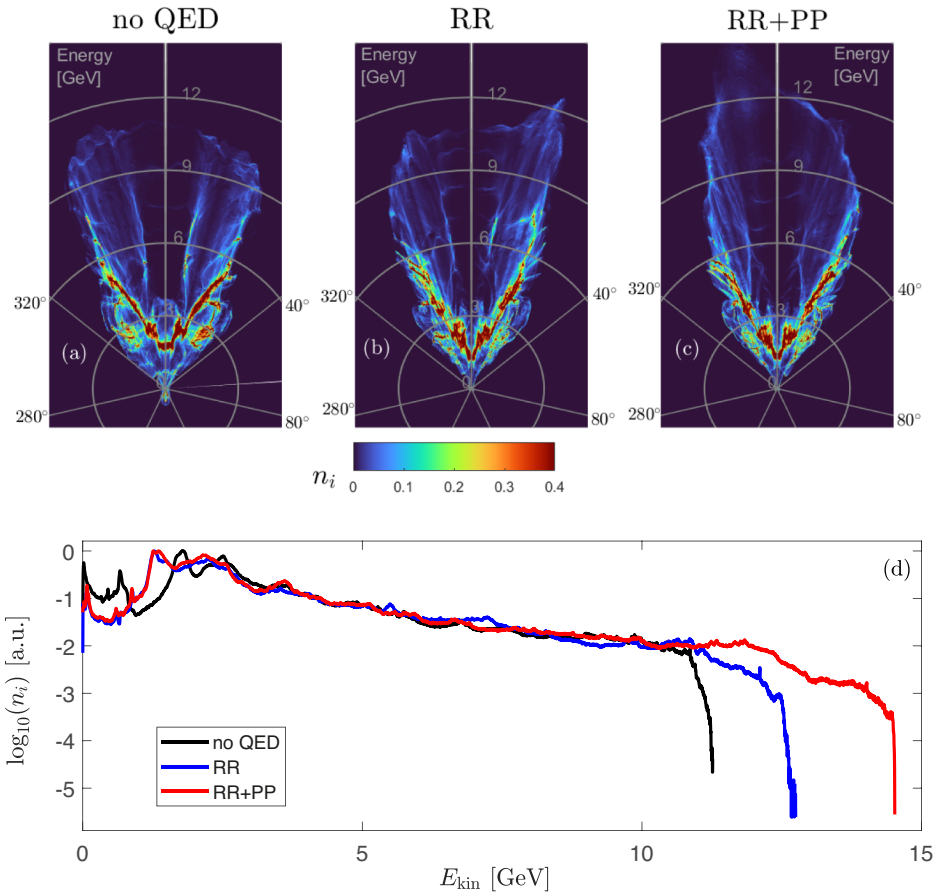

Figure 8. Energy-angle distribution of carbon ions in the BOA phase without the radiation reaction (a), with the radiation reaction (b) and with pair production as well (c) at 130 fs. (d) The angle-averaged ion energy distribution at the same time.

dispersion relation, which has a negative frequency for $k = 0$, matches very well the branch *B* picked up by the fast Fourier transform (FFT) of the longitudinal electric fields from simulation. This points to a lower ion-mode that additionally bestows the high-energy on-axis ions, accelerated at a later time due to mutually interacting angular ion streams. In the dispersion relation of the RBI, with angularly streaming plasma characteristics extracted from 70 fs, when the electronic contributions are allowed to vanish, $n_e = 0$ and $\epsilon_e = 0$, we obtain a quadratic equation giving two real roots. One of the real roots (ω_r) of the perturbation, which would mean non-growing/non-damping oscillation, matches perfectly with the lower frequency root 4 in Figure 7 that lies over branch *B*. This branch gets stronger with QED effects, which hints at growing oscillations between ion streams as they become more forward-directed. These ion oscillations bring the outward bursting ions more towards the axis of laser propagation.

5.3. RBI phase velocity and resonant ion velocities

Figure 8 shows the angle-energy and the θ-averaged ion distribution in the three cases at a later time of 130 fs. The highest energy gained by the ions at this time in the no-QED case is approximately 11.26 GeV, with the RR it is 12.7 GeV (∼12% higher) and with the RR+PP it is 14.52 GeV (∼30% higher). The corresponding ion velocities $v_i = [0.86c, 0.88c, 0.90c]$ are in good agreement with the respective phase velocities of the RBI $v_p \sim [0.84c, 0.89c, 0.91c]$ from simulations (branch *A*) and also with the overplotted phase velocities of the RBI from linear theory $v_p \sim [0.75c, 0.82c, 0.90c]$. This presents some hints on the possible wave-particle acceleration mechanism[17] (see more details in Appendix C). A good agreement can be seen even without including the RR term in the instability calculation because the strong impact of the RR in Stage 1 is actually included via simulations in the form of changes in the distribution function in Stage 2 of the instability development.

6. Conclusion

In conclusion, we investigated the effect of the RR and PP on the ion acceleration where the BOA mechanism may operate. We demonstrate how QED effects can impact the collective plasma behaviour in the early stages of laser–plasma interaction. This may lead to an enhanced phase

https://doi.org/10.1017/hpl.2023.86 Published online by Cambridge University Press

velocity of the RBI in a later BOA stage. However, the spectra presented here could also be explained by an RPA mechanism by taking into account transverse expansion of the target[68], and a more systematic study of the ion electron and ion phase space at a smaller time scale to search for signatures of the RBI could further clarify the nature of the accelerating mechanism. Nonetheless, non-classical effects clearly modify the plasma distribution significantly in this regime and can lead to a gain of higher energy (around 30%) by the ions. The angle of streaming between the transparent target electrons and the forward-directed e^-e^+ pair plasma plays a principal role in plasma dynamics and the consequent high ion energy gain. Measuring the deviations in the experimentally observed particle spectra from classically expected results can help identify or verify QED signatures. Apart from energy enhancement, the simulations presented here also show that with QED effects the highest ion energy signal would be for the particles directed near the laser propagation, whereas without QED effects this would be at an angle appreciably above zero degree. This can be a key signature to verify QED effects. Recent related experimental corroboration of QED effects[69–71] and the advent of ultra-high intensity lasers[32,34,52,72] place these findings in very exciting times.

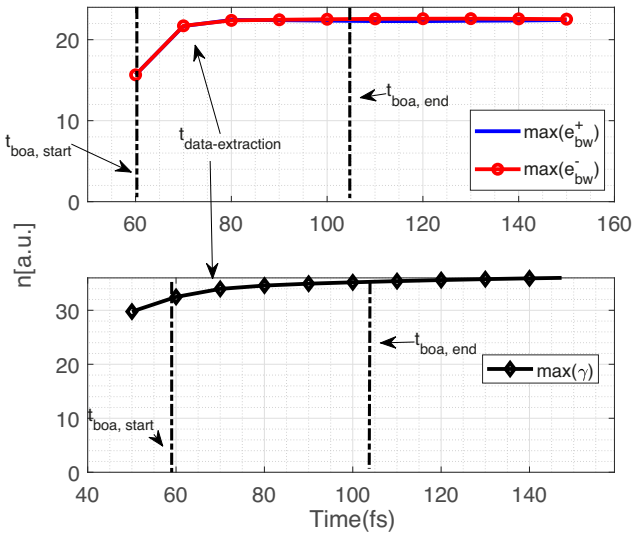

Figure 9. Photons and pairs saturate after which the direct impact of QED effects can be assumed to be less significant. This justifies the dropping of the RR term in the Lorentz force from the Vlasov equation. QED effects are still captured in form of changes in plasma distribution.

Appendices

A. Extraction of plasma characteristics for instability calculation

To extract the plasma characteristics, we choose a time of 70 fs. This is when the onset of the RBI is expected with the target turning transparent and the electrons and ions streaming forward. Figure 9 shows the time evolution of the peak values of the number of photons and pairs produced in the QED cases of the simulation considered in the manuscript. A clear saturation of the number of photons and pairs around 70 fs (Stage 2) implies that the emission of particles is negligible beyond this time and the RR term in the Lorentz force can be safely dropped from the Vlasov equation. It is after this time that the ions experience a boosted acceleration potentially due to the RBI. The QED effects are strong at earlier times (Stage 1) and modify the plasma distribution function that would be used at 70 fs as the initial condition to the instability evolution.

To compute the dispersion relation for the RBI, an initial streaming plasma distribution function,

$$f_{e,i}\left(\overrightarrow{p}\right) = n_0 \delta\left(\overrightarrow{p} - \overrightarrow{P}_0\right), \tag{2}$$

with mean drift $\overrightarrow{P}_0 = \left[P_{0x}, P_{0y}, 0\right]$ (as in Refs. [17, 27]) is perturbed with a small perturbation of the form $\xi = \xi_0 \exp\iota(\overrightarrow{k} \cdot \overrightarrow{x} - \omega t)$. As PIC simulations generate a continuous distribution of plasma particles, to attain plasma values that can fit into this cold distribution we average out the distribution. For this, a normal distribution curve is fitted onto the particle energy distribution at each angle θ_i using the method of non-linear least squares that iteratively minimizes the residue between PIC data and the fitted curve (with a goodness of fit of $R^2 = 0.8 - 0.9$), and the mean is extracted. With this, an average energy $\overline{E}_i$ is determined with an uncertainty of $\pm\Delta E_i$ (limits of 95% confidence interval). This energy and the corresponding particle number $\overline{n}_i$ with uncertainty $\pm\Delta n_i$ is then plotted as a function of θ and the mean angle of flow is determined (see Figure 10). Since the fast moving particles participate in the RBI, cutoffs of 0.1 and 1 GeV are applied on the electron and ion distribution, respectively, while fitting to rule out the target species far from the focal area that is still opaque to the laser.

In this procedure of determining the mean plasma density, energy and angle, the pairs population is also added to the electrons in the QED case. Positrons can also be added here due to presence of charge in the form of e^2 in the dispersion relation (Equation (1)). This addition does not manifest itself as a significant change in the number density of plasma, but rather the average angle of flow of the electron cloud, making it more and more forward-directed, as shown in Section 3.

B. Numerical robustness

B.1. Particle numbers

The 2D simulations were repeated with different numbers of macro-particles per cell $\left(N_{ppc}\right)$ to check the numerical reliability of these results. The maximum ion energies are tabulated in Table 1. The maximum energy gained by the

https://doi.org/10.1017/hpl.2023.86 Published online by Cambridge University Press

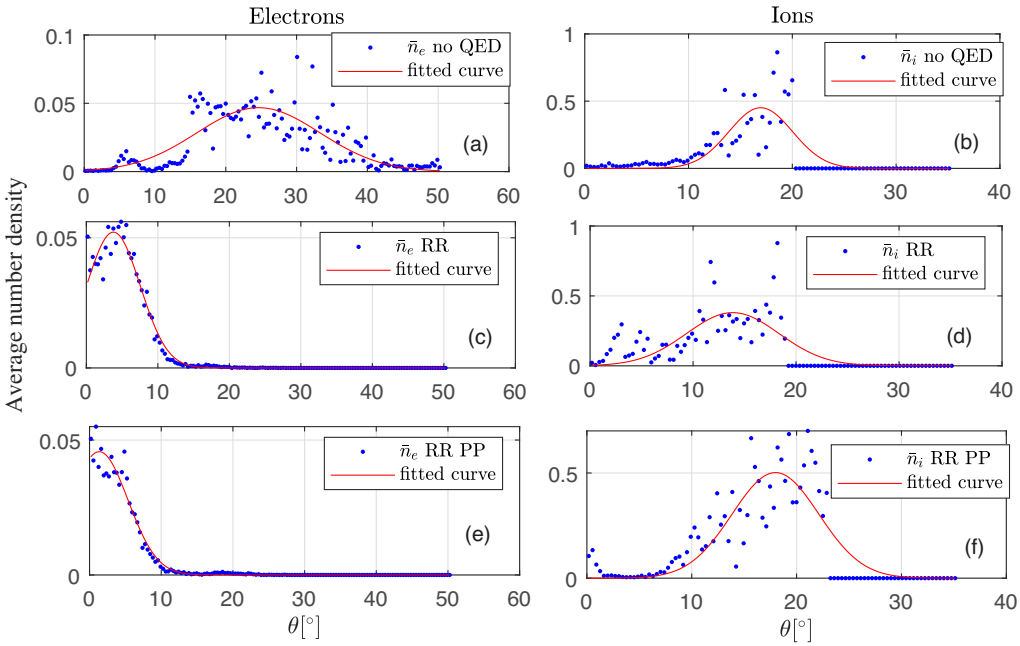

Figure 10. Average number density of electrons (first column) and ions (second column) as a function of the angle.

Table 1. Maximum ion energies in GeV. The percentage change from the no-QED case is tabulated in round brackets in each QED case. All simulations are performed by EPOCH.

N_{ppc}	E_{max}, no QED	E_{max}, RR	E_{max}, RR+PP
20	11.05	13.1 (↑ 18%)	14.33 (↑ 30%)
85[a]	11.26	12.7 (↑ 13%)	14.52 (↑ 29%)
200	11.50	11.76 (↑ 2%)	13.4 (↑ 16%)
300	11.55	12.36 (↑ 7%)	13.15 (↑ 15%)

[a]As in the main text.

ions varies with different numbers of macro-particles, N_{ppc}, even for the no-QED case. With this we prescribe a numerical error bar to the value of maximum energy gained by the ions. At times there is an overlap between the lower end of energy error bar of the QED case and the upper end of the energy error bar of the no-QED case (also including different N_{ppc} values in between the ones in the table). This can also be seen in Table 1 where the ion energy of 11.76 GeV in the RR case almost overlaps with the no-QED case of 11.55 GeV with a different number of particles.

To clearly disentangle these error bars, instead of comparing just the maximum ion energy gained by the fastest ions, we compare energy cutoff of some fth percentile of the ion's high-energy tail. This can be seen in Figure 11. Here the circular data point represents the case discussed in the paper with the error bar due to different numbers of particles. So, for instance, for $f = 92$ the circular data point represents the energy cutoff between the fastest 8% of the particles and the remaining 92% with lower energy. The corresponding error bar originates from the same energy cutoffs of the fastest 8% from the simulations with different numbers of particles. As expected, the energy cutoff of the fastest 8% is

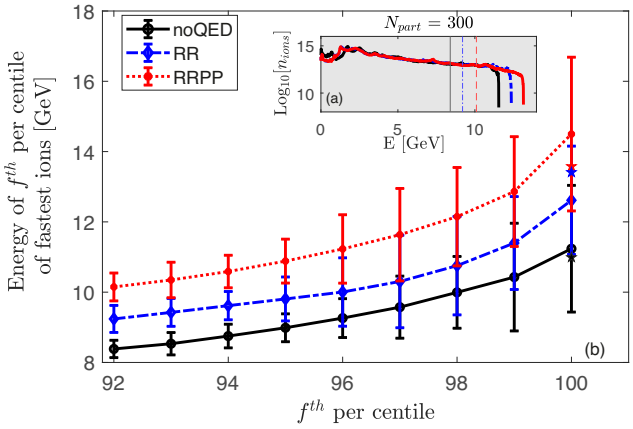

Figure 11. Minimum energy of the fastest 1%−8% of particles of the high-energy tail with an error bar due to different N_{ppc} values.

lower (around 8 GeV) than the fastest 1% (around 11 GeV). Figure 11(a) shows one typical ion energy spectrum with vertical lines marking this energy cutoff of the top 8% ions from the high-energy tail (instead of only the highest energy, which shows much larger numerical variations due to the chosen number of particles). The overlapping error bar due to different particle numbers disentangles at around the 92nd percentile of particles in the high-energy tail, clearly corroborating an energy enhancement with QED effects by 2D simulations.

B.2. From an alternative code: SMILEI

Moreover, to cross-check these findings, we also performed few additional simulations with another PIC code called

https://doi.org/10.1017/hpl.2023.86 Published online by Cambridge University Press

Table 2. Maximum ion energies in GeV. The percentage change from the no-QED case is tabulated in round brackets in each QED case. All simulations are performed by SMILEI.

N_{ppc}	E_{max}, no QED	E_{max}, RR	E_{max}, RR+PP
$84^{\text{dt}>\text{dt}_{\text{QED}}}$	12.40	12.61 (↑ 2%)	13.87 (↑ 12%)
$126^{\text{dt}\sim\text{dt}_{\text{QED}}}$	12.76	14.71 (↑ 15%)	15.00 (↑ 18%)
$210^{\text{dt}\sim\text{dt}_{\text{QED}}}$	12.33	12.48 (↑ 2%)	12.82 (↑ 5%)
$252^{\text{dt}\sim\text{dt}_{\text{QED}}}$	11.23	12.55 (↑ 11%)	12.71 (↑ 14%)

Table 3. Maximum ion energies in GeV with enhanced spatial resolution in SMILEI code and in EPOCH corroborate the trend of energy improvement. Superscript '0' denotes the 'no-QED' case here.

N_{ppc}	dt, dx	E^0_{max}	E_{max}, RR	E_{max}, RR+PP
85^{EPOCH}	0.007 fs, 5.0 nm	11.93	12.63 (↑ 5%)	12.68 (↑ 7%)
85^{EPOCH}	0.006 fs, 3.2 nm	10.99	13.41 (↑ 22%)	13.58 (↑ 24%)
126^{SMILEI}	0.008 fs, 6.0 nm	11.15	11.46 (↑ 3%)	12.42 (↑ 12%)
126^{SMILEI}	0.008 fs, 10 nm	12.76	14.71 (↑ 15%)	15.00 (↑ 18%)

SMILEI[73] in light of some differences observed in the collisions modules of the PIC[74]. First one simulation was carried out with the same number of particles ($N_{\text{ppc}} = 84$) and a spatio-temporal step as in the manuscript (d$t \sim 0.012$ fs). The peak energies are tabulated in the top row of Table 2 and show the same energy enhancement through QED effects. Other simulations with higher numbers of particles and a smaller time step d$t_{\text{pic}} \sim$ d$t_{\text{QED}} \sim 0.007$ fs[75] were also carried out and are tabulated further in Table 2. A typical ion energy spectrum from the simulation with a faster time step and higher particle numbers (126) is shown in Figure 12. Here as well we see the same behaviour of energy enhancement with QED effects, which are well within the error bar of Figure 11.

B.3. Spatial and temporal resolution

In the simulations in Appendix B and that in the manuscript, the time step is chosen as d$t \sim 0.012$ fs. This is larger than yet close to the photon emission time d$t_{\text{QED}} = 0.007$ fs. This is reasonable because around this ratio of dt/d$t_{\text{QED}} \sim 0.58$ it has been shown[75] that the error in energy radiated as photons per particle in Monte Carlo simulations converges to a reasonable accuracy. Nevertheless, we performed one simulation with $N_{\text{ppc}} = 85$ (as in Section 2) but a much smaller time step d$t \sim 0.006$ fs as well (Table 3). The spatial resolution chosen as default by the EPOCH code to ensure fulfilment of the Courant-Friedrichs-Lewy (CFL) criterion gives a cell size of 3.2 nm in both dimensions. The peak energies from this are marked as a star in respective colours in Figure 11 (see on the 100th percentile line) and show around 23% energy enhancement. These values are still well within the prescribed error bar showing that a lower time step would not generate a complete outlier for a typical value of N_{ppc}. Also, in Appendix B and this paper, the spatial resolution was held at 10 nm, which resolves the electron skin depth of 11.25 nm. Additional sets of simulations with finer spatial resolution were also performed from both EPOCH and SMILEI codes. The ion energies show the same trend of energy enhancement and are tabulated in Table 3.

Thus, these 2D simulations successfully capture a clear trend of the enhancement of ion energy by QED effects.

B.4. Pair production

We performed a simulation that includes PP by the BW, trident and Bethe-Heitler (BH) processes. Figure 13 shows how the total number of pairs evolves over time in this laser–solid interaction scenario. Clearly pairs produced by the BW process in the laser-field dominate over the trident process in the laser-field and the BH process in the carbon ion coulombic field. We see from this simulation that BH pairs are about 50 times smaller in number than BW pairs.

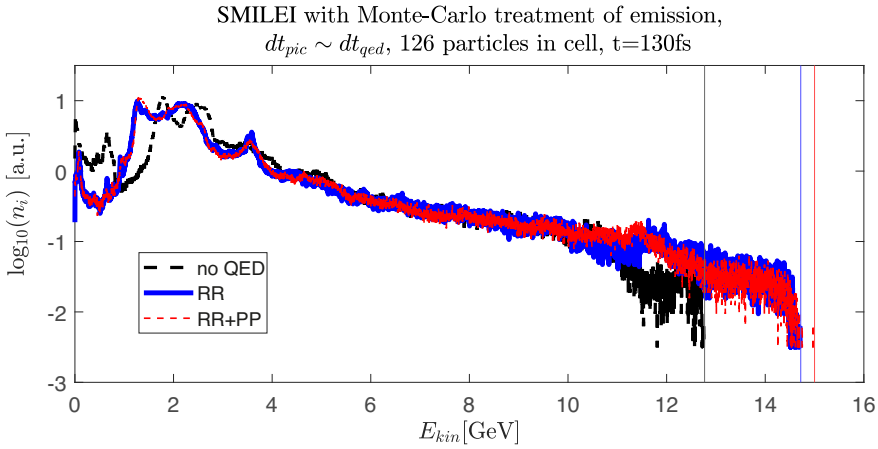

Figure 12. The ion energy distribution at 130 fs from the exactly same scenario in the manuscript when simulated by another PIC code, Smilei[73], shows the same trend and is within the error bar of Figure 11.

https://doi.org/10.1017/hpl.2023.86 Published online by Cambridge University Press

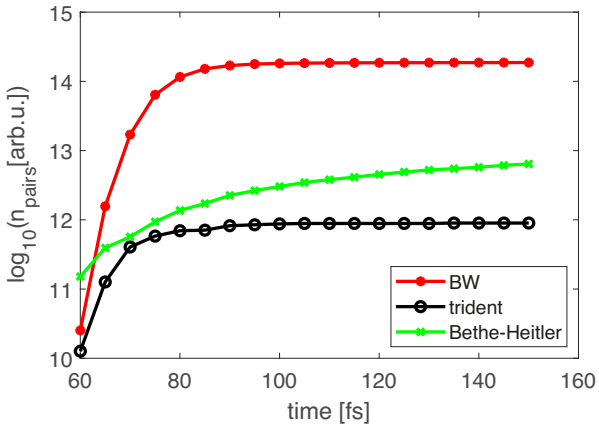

Figure 13. Time evolution of the total pairs produced by the Breit–Wheeler (BW), trident and Bethe–Heitler (BH) processes. This simulation is performed with EPOCH with parameters the same as in Section 2.

The number of tri pairs also increases sharply in the transparency region, like BW pairs, but they are two orders of magnitude (about 200 times) lower than BW pairs.

B.5. Outlook

It should be noted that this work is at the front line of what can be implemented numerically at those extreme parameters, including the PP and RR with corresponding high numerical uncertainties. Future research including code amendments would be advisable for further understanding of the rich complex physics in this region.

C. Phase velocity of the instability and the ion velocities

Figure 14 shows that the ion velocities from the simulations (with the error bar from the above analysis) are very close to the phase velocities of the RBI (with error bars due to uncertainty in data extraction from the simulation),

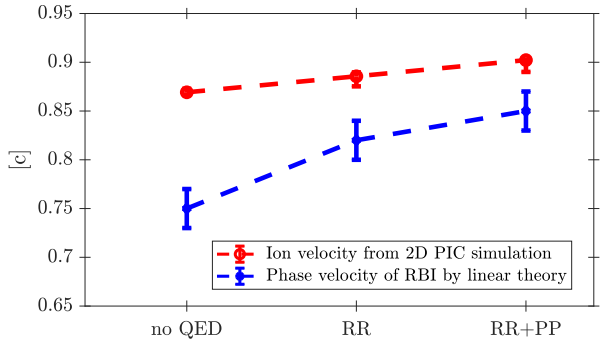

Figure 14. Maximum ion velocities from 2D PIC simulations (red), with the error bar from different numbers of quasi-particles per cell. Phase velocities from the RBI (blue), with error bars due to uncertainty in the data extraction from simulation. It should be noted that the extraction of the plasma characteristics for the instability's phase velocity calculation (blue error bar) has been obtained from the simulation presented in the main text.

implying a possibility of wave-particle Landau resonance in ion acceleration.

D. Stochasticity and ion energies

Figure 15 shows ion energy spectra without the RR (black), with the RR using a corrected Landau–Lifschitz model (sky blue) and with a more accurate Monte Carlo description[51] (dark blue). The ion energy enhancement is observed in both, yet this is to different magnitudes where the Monte Carlo model predicts a larger value of $E_{\max}$. Energy enhancement by stochastic effects captured by the Monte Carlo method is also observed in Ref. [76], where a circularly polarized laser is used to study the RPA of ions. From Figures 4(b) and 4(c) we see that stochastic effects allow electrons to have a larger longitudinal momentum (more than $800m_ec$ in Figure 4(c)) even though the degree of collimation is not significantly different. This highlights the significance of high-energy driver electrons in instability that facilitate a higher energy of ions with stochastic effects.

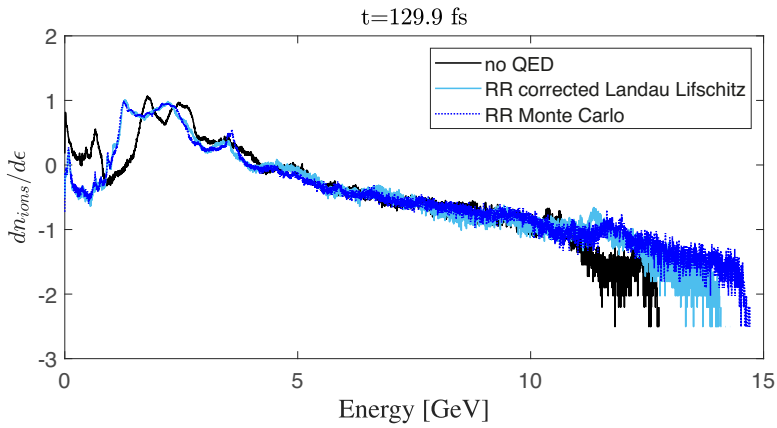

Figure 15. The ion energy spectra from SMILEI without the RR (black), with the RR using the corrected Landau–Lifschitz model that excludes stochasticity (sky blue) and with the more accurate Monte Carlo description (dark blue).

https://doi.org/10.1017/hpl.2023.86 Published online by Cambridge University Press

Acknowledgements

The authors would like to thank Naveen Kumar for suggesting to look into the BOA mechanism for ion acceleration and for his follow-up insightful discussions during the early stage of this work. The authors would like to thank Tom G. Blackburn, Arkady Gonoskov, Joel Magnusson, Brian Reville and Matteo Tamburini for their insightful discussions throughout this work. In particular, we are grateful to Stepan Bulanov and Sergey Bulanov for their insightful comments on the role of the Buneman instability and the influence of the RPA mechanism.

References

1. P. McKenna, K. W. D. Ledingham, T. McCanny, R. P. Singhal, I. Spencer, E. L. Clark, F. N. Beg, K. Krushelnick, M. S. Wei, J. Galy, J. Magill, R. J. Clarke, K. L. Lancaster, P. A. Nofreys, K. Spohr, and R. Chapman, Appl. Phys. Lett. **83**, 2763 (2003).
2. M. Roth, T. E. Cowan, M. H. Key, S. P. Hatchett, C. Brown, W. Fountain, J. Johnson, D. M. Pennington, R. A. Snavely, S. C. Wilks, K. Yasuike, H. Ruhl, F. Pegoraro, S. V. Bulanov, E. M. Campbell, M. D. Perry, and H. Powell, Phys. Rev. Lett. **86**, 436 (2001).
3. J. C. Fernández, B. J. Albright, F. N. Beg, M. E. Foord, B. M. Hegelich, J. J. Honrubia, M. Roth, R. B. Stephens, and L. Yin, Nucl. Fusion **54**, 054006 (2014).
4. M. Roth, D. Jung, K. Falk, N. Guler, O. Deppert, M. Devlin, A. Favalli, J. Fernandez, D. Gautier, M. Geissel, R. Haight, C. E. Hamilton, B. M. Hegelich, R. P. Johnson, F. Merrill, G. Schaumann, K. Schoenberg, M. Schollmeier, T. Shimada, T. Taddeucci, J. L. Tybo, F. Wagner, S. A. Wender, C. H. Wilde, and G. A. Wurden, Phys. Rev. Lett. **110**, 044802 (2013).
5. S. V. Bulanov, T. Esirkepov, V. S. Khoroshkov, A. V. Kuznetsov, and F. Pegoraro, Phys. Lett. Sect. A **299**, 240 (2002).
6. J. Schreiber, P. R. Bolton, and K. Parodi, Rev. Sci. Instrum. **87**, 071101 (2016).
7. S. V. Bulanov, J. J. Wilkens, T. Z. Esirkepov, G. Korn, G. Kraft, S. D. Kraft, M. Molls, and V. S. Khoroshkov, Phys.-Usp. **57**, 1149 (2014).
8. A. Macchi, M. Borghesi, and M. Passoni, Rev. Mod. Phys. **85**, 751 (2013).
9. H. Daido, M. Nishiuchi, and A. S. Pirozhkov, Rep. Prog. Phys. **75**, 056401 (2012).
10. R. A. Snavely, M. H. Key, S. P. Hatchett, T. E. Cowan, M. Roth, T. W. Phillips, M. A. Stoyer, E. A. Henry, T. C. Sangster, M. S. Singh, S. C. Wilks, A. MacKinnon, A. Offenberger, D. M. Pennington, K. Yasuike, A. B. Langdon, B. F. Lasinski, J. Johnson, M. D. Perry, and E. M. Campbell, Phys. Rev. Lett. **85**, 2945 (2000).
11. T. Esirkepov, M. Borghesi, S. V. Bulanov, G. Mourou, and T. Tajima, Phys. Rev. Lett. **92**, 175003 (2004).
12. A. P. L. Robinson, D. H. Kwon, and K. Lancaster, Plasma Phys. Controll. Fusion **51**, 095006 (2009).
13. C. A. J. Palmer, J. Schreiber, S. R. Nagel, N. P. Dover, C. Bellei, F. N. Beg, S. Bott, R. J. Clarke, A. E. Dangor, S. M. Hassan, P. Hilz, D. Jung, S. Kneip, S. P. D. Mangles, K. L. Lancaster, A. Rehman, A. P. L. Robinson, C. Spindloe, J. Szerypo, M. Tatarakis, M. Yeung, M. Zepf, and Z. Najmudin, Phys. Rev. Lett. **108**, 225002 (2012).
14. D. Haberberger, S. Tochitsky, F. Fiuza, C. Gong, R. A. Fonseca, L. O. Silva, W. B. Mori, and C. Joshi, Nat. Phys. **8**, 95 (2012).
15. L. O. Silva, M. Marti, J. R. Davies, R. A. Fonseca, C. Ren, F. S. Tsung, and W. B. Mori, Phys. Rev. Lett. **92**, 015002 (2004).
16. L. Yin, B. J. Albright, B. M. Hegelich, K. J. Bowers, K. A. Flippo, T. J. T. Kwan, and J. C. Fernández, Phys. Plasmas **14**, 056706 (2007).
17. B. J. Albright, L. Yin, K. J. Bowers, B. M. Hegelich, K. A. Flippo, T. J. T. Kwan, and J. C. Fernández, Phys. Plasmas **14**, 094502 (2007).
18. B. M. Hegelich, I. Pomerantz, L. Yin, H. C. Wu, D. Jung, B. J. Albright, D. C. Gautier, S. Letzring, S. Palaniyappan, R. Shah, K. Allinger, R. Hörlein, J. Schreiber, D. Habs, J. Blakeney, G. Dyer, L. Fuller, E. Gaul, E. Mccary, A. R. Meadows, C. Wang, T. Ditmire, and J. C. Fernandez, New J. Phys. **15**, 085015 (2013).
19. A. Henig, S. Steinke, M. Schnürer, T. Sokollik, R. Hörlein, D. Kiefer, D. Jung, J. Schreiber, B. M. Hegelich, X. Q. Yan, J. Meyer-Ter-Vehn, T. Tajima, P. V. Nickles, W. Sandner, and D. Habs, Phys. Rev. Lett. **103**, 245003 (2009).
20. P. Hilz, T. M. Ostermayr, A. Huebl, V. Bagnoud, B. Borm, M. Bussmann, M. Gallei, J. Gebhard, D. Haffa, J. Hartmann, T. Kluge, F. H. Lindner, P. Neumayr, C. G. Schaefer, U. Schramm, P. G. Thirolf, T. F. Rösch, F. Wagner, B. Zielbauer, and J. Schreiber, Nat. Commun. **9**, 423 (2018).
21. F. Wan, W.-Q. Wang, Q. Zhao, H. Zhang, T.-P. Yu, W.-M. Wang, W.-C. Yan, Y.-T. Zhao, K. Z. Hatsagortsyan, C. H. Keitel, S. V. Bulanov, and J.-X. Li, Phys. Rev. Appl. **17**, 024049 (2022).
22. A. Higginson, R. J. Gray, M. King, R. J. Dance, S. D. R. Williamson, N. M. H. Butler, R. Wilson, R. Capdessus, C. Armstrong, J. S. Green, S. J. Hawkes, P. Martin, W. Q. Wei, S. R. Mirfayzi, X. H. Yuan, S. Kar, M. Borghesi, R. J. Clarke, D. Neely, and P. McKenna, Nat. Commun. **9**, 724 (2018).
23. S. Keppler, N. Elkina, G. A. Becker, J. Hein, M. Hornung, M. Mäusezahl, C. Rödel, I. Tamer, M. Zepf, and M. C. Kaluza, Phys. Rev. Res. **4**, 013065 (2022).
24. J. Schreiber, F. Bell, F. Grüner, U. Schramm, M. Geissler, M. Schnürer, S. Ter-Avetisyan, B. M. Hegelich, J. Cobble, E. Brambrink, J. Fuchs, P. Audebert, and D. Habs, Phys. Rev. Lett. **97**, 045005 (2006).
25. A. Henig, D. Kiefer, K. Markey, D. C. Gautier, K. A. Flippo, S. Letzring, R. P. Johnson, T. Shimada, L. Yin, B. J. Albright, K. J. Bowers, J. C. Fernández, S. G. Rykovanov, H. C. Wu, M. Zepf, D. Jung, V. K. Liechtenstein, J. Schreiber, D. Habs, and B. M. Hegelich, Phys. Rev. Lett. **103**, 045002 (2009).
26. L. Yin, B. J. Albright, D. Jung, R. C. Shah, S. Palaniyappan, K. J. Bowers, A. Henig, J. C. Fernndez, and B. M. Hegelich, Phys. Plasmas **18**, 063103 (2011).
27. M. King, R. J. Gray, H. W. Powell, R. Capdessus, and P. McKenna, Plasma Phys. Control. Fusion **59**, 014003 (2017).
28. M. King, R. J. Gray, H. W. Powell, D. A. MacLellan, B. Gonzalez-Izquierdo, L. C. Stockhausen, G. S. Hicks, N. P. Dover, D. R. Rusby, D. C. Carroll, H. Padda, R. Torres, S. Kar, R. J. Clarke, I. O. Musgrave, Z. Najmudin, M. Borghesi, D. Neely, and P. McKenna, Nucl. Instrum. Methods Phys. Res. Sect. A **829**, 163 (2016).
29. G. M. Petrov, C. McGuffey, A. G. R. Thomas, K. Krushelnick, and F. N. Beg, Plasma Phys. Controll. Fusion **59**, 075003 (2017).
30. F. Wagner, S. Bedacht, V. Bagnoud, O. Deppert, S. Geschwind, R. Jaeger, A. Ortner, A. Tebartz, B. Zielbauer, D. H. H. Hoffmann, and M. Roth, Phys. Plasmas **22**, 063110 (2015).
31. N. P. Dover, T. Ziegler, S. Assenbaum, C. Bernert, S. Bock, F.-E. Brack, T. E. Cowan, E. J. Ditter, M. Garten, L. Gaus, I. Goethel, G. S. Hicks, H. Kiriyama, T. Kluge, J. K. Koga, A. Kon, K. Kondo, S. Kraft, F. Kroll, H. F. Lowe, J. Metzkes-Ng, T. Miyatake, Z. Najmudin, T. Püschel, M. Rehwald, M. Reimold, H. Sakaki, H.-P. Schlenvoigt, K. Shiokawa, M. E. P.

https://doi.org/10.1017/hpl.2023.86 Published online by Cambridge University Press

Umlandt, U. Schramm, K. Zeil, and M. Nishiuchi, Light Sci. Appl. **12**, 71 (2023).
32. D. N. Papadopoulos, J. P. Zou, C. Le Blanc, G. Chériaux, P. Georges, F. Druon, G. Mennerat, P. Ramirez, L. Martin, A. Fréneaux, A. Beluze, N. Lebas, P. Monot, F. Mathieu, and P. Audebert, High Power Laser Sci. Eng. **4**, e34 (2016).
33. V. Bagnoud, B. Aurand, A. Blazevic, S. Borneis, C. Bruske, B. Ecker, U. Eisenbarth, J. Fils, A. Frank, E. Gaul, S. Goette, C. Haefner, T. Hahn, K. Harres, H. M. Heuck, D. Hochhaus, D. H. H. Hoffmann, D. Javorková, H. J. Kluge, T. Kuehl, S. Kunzer, M. Kreutz, T. Merz-Mantwill, P. Neumayer, E. Onkels, D. Reemts, O. Rosmej, M. Roth, T. Stoehlker, A. Tauschwitz, B. Zielbauer, D. Zimmer, and K. Witte, Appl. Phys. B **100**, 137 (2010).
34. S. Gales, K. A. Tanaka, D. L. Balabanski, F. Negoita, D. Stutman, O. Tesileanu, C. A. Ur, D. Ursescu, I. Andrei, S. Ataman, M. O. Cernaianu, L. D'Alessi, I. Dancus, B. Diaconescu, N. Djourelov, D. Filipescu, P. Ghenuche, D. G. Ghita, C. Matei, K. Seto, M. Zeng, and N. V. Zamfir, Rep. Prog. Phys. **81**, 094301 (2018).
35. Z. Li, Y. Kato, and J. Kawanaka, Sci. Rep. **11**, 151 (2021).
36. J. Schwinger, Phys. Rev. **82**, 664 (1951).
37. G. Breit and J. A. Wheeler, Phys. Rev. **46**, 1087 (1934).
38. S. Bhadoria and N. Kumar, Phys. Rev. E **99**, 043205 (2019).
39. M. Tamburini, F. Pegoraro, A. Di Piazza, C. H. Keitel, and A. Macchi, New J. Phys. **12**, 123005 (2010).
40. M. Tamburini, F. Pegoraro, A. Di Piazza, C. H. Keitel, T. V. Liseykina, and A. Macchi, Nucl. Instrum. Methods Phys. Res. Sect. A **653**, 181 (2011).
41. E. Wallin, A. Gonoskov, C. Harvey, O. Lundh, and M. Marklund, J. Plasma Phys. **83**, 905830208 (2017).
42. D. D. Sorbo, D. R. Blackman, R. Capdessus, K. Small, C. Slade-Lowther, W. Luo, M. J. Duff, A. P. L. Robinson, P. McKenna, Z. M. Sheng, J. Pasley, and C. P. Ridgers, New J. Phys. **20**, 033014 (2018).
43. R. Capdessus, L. Gremillet, and P. McKenna, New J. Phys. **22**, 113003 (2020).
44. M. Tamburini, T. V. Liseykina, F. Pegoraro, and A. Macchi, Phys. Rev. E **85**, 016407 (2012).
45. M. Chen, A. Pukhov, T.-P. Yu, and Z.-M. Sheng, Plasma Phys. Control. Fusion **53**, 014004 (2010).
46. R. Capdessus and P. McKenna, Phys. Rev. E **91**, 053105 (2015).
47. E. G. Gelfer, A. M. Fedotov, and S. Weber, New J. Phys. **23**, 095002 (2021).
48. S. S. Bulanov, E. Esarey, C. B. Schroeder, S. V. Bulanov, T. Z. Esirkepov, M. Kando, F. Pegoraro, and W. P. Leemans, Phys. Plasmas **23**, 056703 (2016).
49. D. J. Stark, L. Yin, and B. J. Albright, Phys. Plasmas **25**, 062107 (2018).
50. J. G. Kirk, A. R. Bell, and I. Arka, Plasma Phys. Control. Fusion **51**, 085008 (2009).
51. R. Duclous, J. G. Kirk, and A. R. Bell, Plasma Phys. Control. Fusion **53**, 015009 (2010).
52. J. W. Yoon, Y. G. Kim, I. W. Choi, J. H. Sung, H. W. Lee, S. K. Lee, and C. H. Nam, Optica **8**, 630 (2021).
53. D. J. Stark, L. Yin, B. J. Albright, and F. Guo, Phys. Plasmas **24**, 053103 (2017).
54. H. Bethe and W. Heitler, Royal Soc. **146**, 83 (1934).
55. H. J. Bhabha and W. Heitler, Royal Soc. **152**, 559 (1935).
56. J. W. Shearer, J. Garrison, J. Wong, and J. E. Swain, Phys. Rev. A **8**, 1582 (1973).
57. T. Beier, Phys. Rep. **339**, 79 (2000).
58. Y. He, T. G. Blackburn, T. Toncian, and A. V. Arefiev, Commun. Phys. **4**, 139 (2021).
59. S. Bhadoria, T. Blackburn, A. Gonoskov, and M. Marklund, Phys. Plasmas **29**, 093109 (2022).
60. S. S. Bulanov, A. Brantov, V. Y. Bychenkov, V. Chvykov, G. Kalinchenko, T. Matsuoka, P. Rousseau, S. Reed, V. Yanovsky, D. W. Litzenberg, K. Krushelnick, and A. Maksimchuk, Phys. Rev. E **78**, 026412 (2008).
61. P. K. Singh, F.-Y. Li, C.-K. Huang, A. Moreau, R. Hollinger, A. Junghans, A. Favalli, C. Calvi, S. Wang, Y. Wang, H. Song, J. J. Rocca, R. E. Reinovsky, and S. Palaniyappan, Nat. Commun. **13**, 54 (2022).
62. Z. Gong, F. Mackenroth, X. Q. Yan, and A. V. Arefiev, Sci. Rep. **9**, 17181 (2019).
63. N. Neitz and A. Di Piazza, Phys. Rev. Lett. **111**, 054802 (2013).
64. J. G. Kirk, A. R. Bell, and C. P. Ridgers, Plasma Phys. Control. Fusion **55**, 095016 (2013).
65. L. Yin, B. J. Albright, K. J. Bowers, D. Jung, J. C. Fernández, and B. M. Hegelich, Phys. Rev. Lett. **107**, 045003 (2011).
66. $[n_e, \theta_e, \epsilon_e]^0 = [0.0026 n_0, 24°, 0.3420\ \text{GeV}]$,
$[n_i, \theta_i, \epsilon_i]^0 = [0.0404 n_0, 16.9°, 1.914\ \text{GeV}]$;
$[n_e, \theta_e, \epsilon_e]^{\text{RR}} = [0.0046 n_0, 8.2°, 0.3925\ \text{GeV}]$,
$[n_i, \theta_i, \epsilon_i]^{\text{RR}} = [0.049 n_0, 13.8°, 2.03\ \text{GeV}]$;
$[n_e, \theta_e, \epsilon_e]^{\text{RR+PP}} = [0.0032 n_0, 5.1°, 0.4128\ \text{GeV}]$,
$[n_i, \theta_i, \epsilon_i]^{\text{RR+PP}} = [0.0591 n_0, 17.9°, 2.01\ \text{GeV}]$; with $n_{e,i,0}$, $\epsilon_{e,i}$ being the electron, ion and the initialized particle density and energies, respectively.
67. D. J. Stark, L. Yin, B. J. Albright, W. Nystrom, and R. Bird, Phys. Plasmas **25**, 043114 (2018).
68. Private communication with S.S. Bulanov and S.V. Bulanov.
69. K. Poder, M. Tamburini, G. Sarri, A. Di Piazza, S. Kuschel, C. D. Baird, K. Behm, S. Bohlen, J. M. Cole, D. J. Corvan, M. Duff, E. Gerstmayr, C. H. Keitel, K. Krushelnick, S. P. D. Mangles, P. McKenna, C. D. Murphy, Z. Najmudin, C. P. Ridgers, G. M. Samarin, D. R. Symes, A. G. R. Thomas, J. Warwick, and M. Zepf, Phys. Rev. X **8**, 031004 (2018).
70. G. Sarri, K. Poder, J. M. Cole, W. Schumaker, A. Di Piazza, B. Reville, T. Dzelzainis, D. Doria, L. A. Gizzi, G. Grittani, S. Kar, C. H. Keitel, K. Krushelnick, S. Kuschel, S. P. D. Mangles, Z. Najmudin, N. Shukla, L. O. Silva, D. Symes, A. G. R. Thomas, M. Vargas, J. Vieira, and M. Zepf, Nat. Commun. **6**, 6747 (2015).
71. J. M. Cole, K. T. Behm, E. Gerstmayr, T. G. Blackburn, J. C. Wood, C. D. Baird, M. J. Duff, C. Harvey, A. Ilderton, A. S. Joglekar, K. Krushelnick, S. Kuschel, M. Marklund, P. McKenna, C. D. Murphy, K. Poder, C. P. Ridgers, G. M. Samarin, G. Sarri, D. R. Symes, A. G. R. Thomas, J. Warwick, M. Zepf, Z. Najmudin, and S. P. D. Mangles, Phys. Rev. X **8**, 011020 (2018).
72. C. N. Danson, C. Haefner, J. Bromage, T. Butcher, J.-C. F. Chanteloup, E. A. Chowdhury, A. Galvanauskas, L. A. Gizzi, J. Hein, D. I. Hillier, N. W. Hopps, Y. Kato, E. A. Khazanov, R. Kodama, G. Korn, R. Li, Y. Li, J. Limpert, J. Ma, C. H. Nam, D. Neely, D. Papadopoulos, R. R. Penman, L. Qian, J. J. Rocca, A. A. Shaykin, C. W. Siders, C. Spindloe, S. Szatmári, R. M. G. M. Trines, J. Zhu, P. Zhu, and J. D. Zuegel, High Power Laser Sci. Eng. **7**, e54 (2019).
73. J. Derouillat, A. Beck, F. Pérez, T. Vinci, M. Chiaramello, A. Grassi, M. Flé, G. Bouchard, I. Plotnikov, N. Aunai, J. Dargent, C. Riconda, and M. Grech, Comput. Phys. Commun. **222**, 351 (2018).
74. S. Bhadoria, N. Kumar, and C. H. Keitel, arXiv:1707.03309v2 (2019).
75. C. P. Ridgers, J. G. Kirk, R. Duclous, T. G. Blackburn, C. S. Brady, K. Bennett, T. D. Arber, and A. R. Bell, J. Comput. Phys. **260**, 273 (2014).
76. F. Wan, K. Xue, Z.-K. Dou, K. Z. Hatsagortsyan, W. Yan, D. Khikhlukha, S. V. Bulanov, G. Korn, Y.-T. Zhao, Z.-F. Xu, and J.-X. Li, Plasma Phys. Control. Fusion **61**, 084010 (2019).

https://doi.org/10.1017/hpl.2023.86 Published online by Cambridge University Press